

Application of scattering chaos to particle transport in a hydrodynamical flow

C. Jung

Fachbereich Physik, Universität Bremen, 28359 Bremen, Germany

T. Tél

Institute for Theoretical Physics, Eötvös University, H-1088 Budapest, Puskin u. 5-7, Hungary

E. Ziemniak

Ruhr-Universität Bochum, 44801 Bochum, Germany

(Received 2 June 1993; accepted for publication 14 October 1993)

The dynamics of a passive particle in a hydrodynamical flow behind a cylinder is investigated. The velocity field has been determined both by a numerical simulation of the Navier–Stokes flow and by an analytically defined model flow. To analyze the Lagrangian dynamics, we apply methods coming from chaotic scattering: periodic orbits, time delay function, decay statistics. The asymptotic delay time statistics are dominated by the influence of the boundary conditions on the wall and exhibit algebraic decay. The short time behavior is exponential and represents hyperbolic effects.

I. INTRODUCTION

The passive transport of particles in hydrodynamical flows provides a nice application of the concept of chaos. The principal objects of chaotic dynamics are defined in phase space and are in general not directly accessible to our perception. The specific feature of passive advection in a two-dimensional time dependent flow is that the phase space of the particle dynamics *coincides* then with the configuration space. The phase space structures thus become observable by the naked eye. Incompressibility of the flow implies phase volume conservation and, consequently, Hamiltonian dynamics. The case of chaotic particle transport in *closed* flows provides an example of the so-called *permanent Lagrangian turbulence*. This has been intensively studied in the past years,^{1–14} which has led to a better understanding of the problem of mixing and stirring. Recently, similar ideas have been applied to *open* flows^{15–18} which might be relevant to mixing in continuous flow reactors. The chaotic motion of a passive particle can then be considered as a realization of *transient Lagrangian turbulence*. The Hamiltonian structure of the dynamics, the openness of the flow, and the asymptotic simplicity of the motion make advection analogous to particle *scattering*.

In particular, we consider the case of a straight channel containing a circular obstacle. An incompressible viscous fluid moves through the channel from left to right. The flow is characterized by two free parameters, the Reynolds number and the aspect ratio, i.e. the ratio between the diameter of the obstacle and the width of the channel. We assume that the velocity of the fluid is sufficiently small that far in front and far behind the cylinder a parabolic velocity profile is created. Only in the direct vicinity behind the cylinder we find a more complicated flow pattern which depends sensitively on the Reynolds number Re at a given aspect ratio. In the following we concentrate on the range of Reynolds numbers where an exactly *time periodic velocity field* occurs.

Behind the cylinder, vortices are created. Later they

detach from the cylinder and drift along the channel. After some distance, they are suppressed by viscosity. Therefore we obtain a typical von Kármán vortex street of finite length. If the flow is confined in a narrow channel (narrow means that the aspect ratio is not very small compared to one), then the vortex street is strongly damped and quite short. We will study the case in which we have at most two different vortices at one instant of time. A similar problem with compressible fluid has been treated in the paper of Shariff, Pulliam, and Ottino¹⁷ by computing invariant manifolds of some singular points on the cylinder's surface and of a period one orbit in the wake. In the incompressible case, the Lagrangian dynamics is of Hamiltonian nature and a direct analogy with particle scattering can be used.

It is known from the theory of chaotic scattering^{19–24} that the complicated motion is organized around a *nonattractive chaotic set*, sometimes called chaotic saddle, which is invariant. This set consists of all the periodic orbits lying in the interaction region and their heteroclinic and homoclinic connections. The aim of scattering methods is to find out the structures in the interaction region by asymptotic measurements. A study of the scattering process provides thus the possibility of obtaining the important characteristics of the chaotic set and, in particular, it shows the influence of nonhyperbolic effects which have not been studied in detail in Ref. 18.

It is also known from earlier studies of chaotic scattering that some basic periodic orbits play a fundamental role. More complicated ones turn out to be shadowed by these basic ones which means that any periodic orbit can be built up from segments of the basic periodic orbits. Long-lived scattering trajectories come close to the periodic ones and, consequently, their segments inside the interaction region can also be shadowed by the basic periodic orbits.^{25–27}

In the hydrodynamical case, the investigation of the shortest periodic orbits generated by the vortices leads to the conclusion that they alone are not sufficient for carrying out the shadowing process. In addition, the wall of the

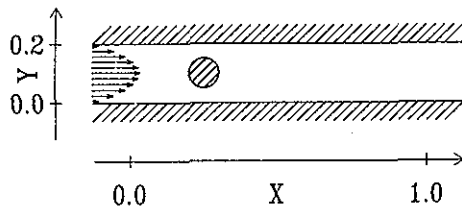


FIG. 1. Geometry of the channel and the cylinder in it. The arrows inside the channel indicate the incoming parabolic velocity profile.

obstacle consisting of a continuum of parabolic points has to be included as it acts like a further basic periodic orbit. In fact, very long periodic orbits can come arbitrarily close to the wall. So we can define two components of the invariant set: the short hyperbolic orbits as well as the ones shadowed by them alone on the one hand, and the wall as well as periodic orbits shadowed partially by the wall on the other hand.

In order to follow the dynamics of the passive transport, the velocity field is needed as input data. The principal approach is a solution of the Navier–Stokes equations which is only numerically possible in this problem. Because of the restriction in the computer resources and resolution we constructed an analytical model of the streamfunction which contains all qualitative features of the Navier–Stokes flow and provides the opportunity to have very good resolution.

The paper is organized as follows: Sec. II contains the results obtained by using the numerically determined Navier–Stokes flow. Next (Sec. III), the model streamfunction is presented and the results are compared on large scale with the previous approach. The most important periodic orbits and their influence on scattering trajectories are discussed in Sec. IV. The fractal properties of the time delay function, and the extraction of the hyperbolic features from it are described in Secs. V and VI, respectively. Sec. VII contains discussions and final remarks.

II. DYNAMICS IN THE NAVIER–STOKES FLOW

In this section we consider the Navier–Stokes flow in an infinite channel of width w with a circular cylinder of radius R placed into the middle of the channel. We will consider sufficiently small Reynolds numbers Re only, for which the flow is essentially two dimensional. As coordinates in the plane we use x and y , where x is parallel to the axis of the channel and y is perpendicular to it. The walls of the channel are at $y=0$ and at $y=w=0.2$. The middle of the cylinder is placed at $x_c=0.25$, $y_c=0.1$, its radius is chosen to be $R=0.05$.

Let the velocity components of the fluid in x and y direction be u and v , respectively. Then for $x \ll x_c=0.25$ and for $x \gg x_c=0.25$ we find

$$u(x,y) = u_0 y(w-y), \quad (1)$$

$$v(x,y) \equiv 0. \quad (2)$$

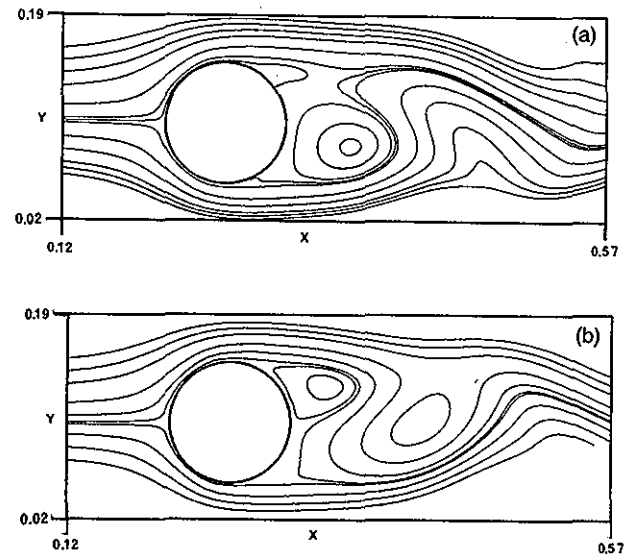


FIG. 2. Streamlines of the flow for $Re=250$, $r=0.25$ at time $t \bmod T_c$, where $t=0$ in part (a), and $t = T_c/4$ in part (b). The reader can obtain the streamlines for $t=T_c/2$ and $t=3T_c/4$ by reflecting the plot of parts (a) and (b), respectively, about the channel's symmetry axis, as follows from Eqs. (3) and (4).

The quantity u_0 has been given the value $u_0 = 6/w^2$ such that the total incoming flow is $\int_0^w u(x,y) dy = w$, i.e. the mean velocity u_{av} equals 1. Figure 1 shows the geometry of the channel and the incoming parabolic velocity profile. In the numerical solutions of the Navier–Stokes equation it turns out that the parabolic velocity profile is valid rather close to the cylinder and so it was sufficient for the following to choose this profile as initial condition along the line $x=0.0$.

We take the viscosity ν of the fluid such that the Reynolds number $Re=2Ru_{av}/\nu$ is in a range where the velocity field is periodic in time with some period T_c at a fixed aspect ratio $r=R/w$. Our unit of time is given by the quotient between the unit of length and u_{av} . All numerical results shown below are obtained for $Re=250$ and $r=0.25$ which leads to $T_c=1.107$. Similar numerical results for $Re=80$ are given in Ref. 18. The Navier–Stokes equation has been solved by a numerical method described in Ref. 28. A grid of size 42×202 in position space has been used and the average temporal resolution provided by the numerical procedure was $0.003 \cdot T_c$. The relaxation to the asymptotic periodic behavior at a given Re and r required a CPU time of several hours on a vector machine. As input for the Lagrange dynamics this velocity field was stored over half a time period on an equidistant space-time grid where the time step $0.03 \cdot T_c$ has been chosen. Several tests have been carried out to check the grid independence (in space and time) of the Navier–Stokes solution and the reliability of the resulting particle dynamics.

By the simultaneous presence of the temporal periodicity of the flow field and the reflectional symmetry along the line $y=w/2=0.1$ of the geometry, the velocity field has the following symmetry:

$$u(x,y,t) = u(x,w-y,t+T_c/2), \quad (3)$$

$$v(x,y,t) = -v(x,w-y,t+T_c/2). \quad (4)$$

Because of the incompressibility of the fluid, there exists a time dependent streamfunction $\psi(x,y,t)$ such that

$$u(x,y,t) = \frac{\partial}{\partial y} \psi(x,y,t), \quad (5)$$

$$v(x,y,t) = -\frac{\partial}{\partial x} \psi(x,y,t) \quad (6)$$

for all x, y, t . The level lines of ψ for fixed t are the streamlines of the flow. Figure 2 gives a plot of the streamlines for $Re=250$ at time $t=0 \bmod T_c$ and at time $t=T_c/4 \bmod T_c$ where the zero of time has been chosen arbitrarily. If the velocity field would be stationary, the streamlines would coincide with the trajectories of the fluid particles.

From Fig. 2 and the symmetry properties of the flow, "we can imagine" the time development of the velocity field. Behind the cylinder two vortices are created within any time interval of length T_c , one in the upper half and the other one in the lower half of the channel. These two vortices are delayed by a time $T_c/2$. The vortices first grow in size, then they separate from the cylinder and start to drift along the channel. Now the viscosity of the fluid and the presence of the walls of the channel become important for their destabilization and destruction after a short length of travel.

Consider a passive marker particle which is placed into the fluid at time $t=t_{in}$ at position $x=x_{in}, y=y_{in}$, and let it move with the fluid through the channel. The trajectory of this particle is the solution of the following equations of motion:

$$\frac{d}{dt} x(t) = u(x,y,t) = \frac{\partial}{\partial y} \psi(x,y,t), \quad (7)$$

$$\frac{d}{dt} y(t) = v(x,y,t) = -\frac{\partial}{\partial x} \psi(x,y,t). \quad (8)$$

Equations (7) and (8) have exactly the same structure as the canonical equations of motion for a particle moving along one-dimensional position space without any friction under the influence of an explicitly time dependent force. We make the following identifications: $x \rightarrow q$ where q is the position of the particle, $y \rightarrow p$ where p is the canonically conjugate momentum of the particle, $\psi(x,y,t) \rightarrow H(q,p,t)$ where H is the explicitly time dependent Hamiltonian of the dynamics. Accordingly, the plot of the streamlines as shown in Fig. 2 can also be interpreted as the level lines of the Hamiltonian at fixed time. For $|x| \rightarrow \infty$, ψ does not really depend on either x or t , but on y only. In the same way for $|q| \rightarrow \infty$, H does not depend on either q or t , but on p only. Therefore, asymptotically the particle moves with a constant speed and we can view the limit $q \rightarrow \pm \infty$ or $x \rightarrow \pm \infty$ as the asymptotic limit of scattering theory.

It is well known that explicitly time dependent Hamiltonian systems with one degree of freedom can exhibit chaotic behavior of essentially the same type as autonomous systems with 2 degrees of freedom. If the system is open as in the present case, almost all trajectories come in from the

incoming asymptotic region. They may exhibit complicated motion for a finite time in the region in which the dynamics is really time dependent, and disappear again into the outgoing asymptotic region. If the dynamics is chaotic at all, it can only be in the form of transient chaos²¹ (scattering chaos).

For a scattering system it is essential to give a proper labeling of asymptotes. In our system this can be done as follows: pick a particular value x_{in} of x in the incoming asymptotic region (in our examples we shall take $x_{in}=0.02$) and record the y -coordinate and the time, t_{in} , modulo T_c at which the trajectory coming from $-\infty$ crosses the line $x=x_{in}$. These two numbers y_{in} and t_{in} label any incoming asymptote uniquely.

A clear criterion for transient chaos is the occurrence of a fractal set of singularities in the *time delay function*.²⁹ In our system this means in detail: take a one-dimensional subset of initial asymptotes, e.g. fix y_{in} , scan t_{in} , and plot the time Dt which the particle needs to reach the outgoing asymptotic region, e.g. the line $x=1.0$. If the system exhibits transient chaos, then for appropriately chosen values of y_{in} this function has infinities on a fractal set along the t_{in} -axis and has intervals of continuity between the gaps of the fractal set.

Figure 3(a) displays a representative example of Dt as function of t_{in} . We see smooth parts and places where the function shows rapid changes, which are not well resolved on this scale. Figure 3(b) gives a magnification with improved resolution of a part of Fig. 3(a), and Fig. 3(c) gives a further magnification of an even smaller part. We see a typical fractal construction: on any level of the hierarchy there are intervals of continuity and unresolved regions in between. On the next level we find new intervals of continuity inside the so far unresolved parts. After every step of this construction there remain even smaller unresolved parts than in the previous step. The Cantor set itself is the set of accumulation points of the boundaries of intervals of continuity. From level to level in this hierarchy the value of Dt increases and on the fractal set itself the value of Dt is infinite.

In this system there are two different mechanism by means of which the time delay of trajectories can become large. Now we describe these two mechanisms and present in Fig. 4 some plots of particle trajectories illustrating them. First, the particle can approach the wall of the cylinder, where the velocity field goes to zero. The big structures in the delay function presented in Fig. 3(a) are caused by the approach of the particle to the wall of the cylinder from the front side. Then the particle passes along the cylinder wall with very small velocity until it separates again on the back side. Such a trajectory is shown in Fig. 4(a). In addition, the particle can come back to the cylinder wall from the rear side after it has performed any other type of motion in the vicinity of the cylinder. Such a case is shown in Fig. 4(b). The most interesting part of this trajectory is repeated in magnification in Fig. 4(c). Here we see in more detail how the particle approaches the back side of the cylinder after it has run through some loops behind the cylinder. It also illustrates, that the particle can

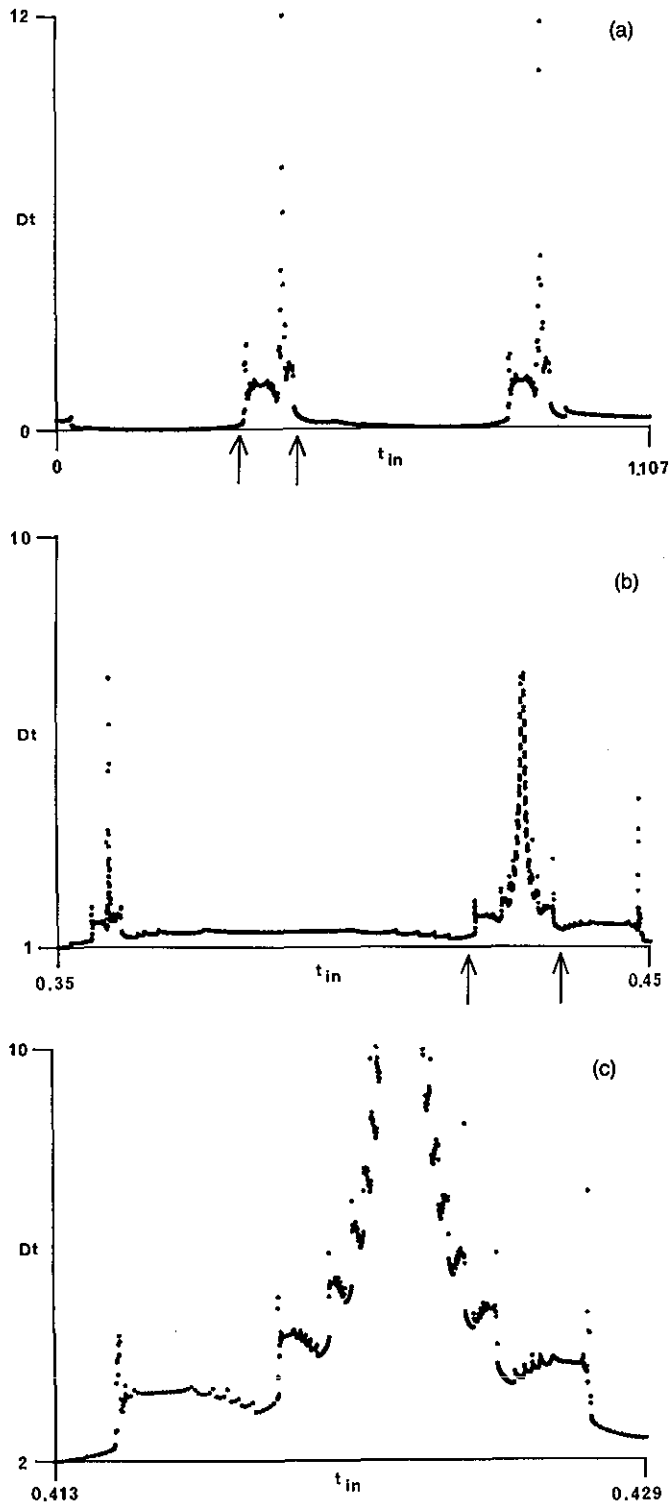


FIG. 3. Plot of the time delay function $Dt(t_{in})$ for $y_{in}=0.0995$. Part (a) shows this function on its whole domain. Part (b) is a magnification of one of the small intervals containing singularities. Part (c) shows a further magnification. The arrows in parts (a) and (b) show the boundaries of the intervals displayed in parts (b) and (c), respectively.

come into the vortex region behind the cylinder and be trapped and whirled around by the vortices for a while. Examples for this behavior can also be seen in Figs. 4(b), 4(d), and 4(e). For comparison the shortest periodic orbits are presented in Fig. 5.

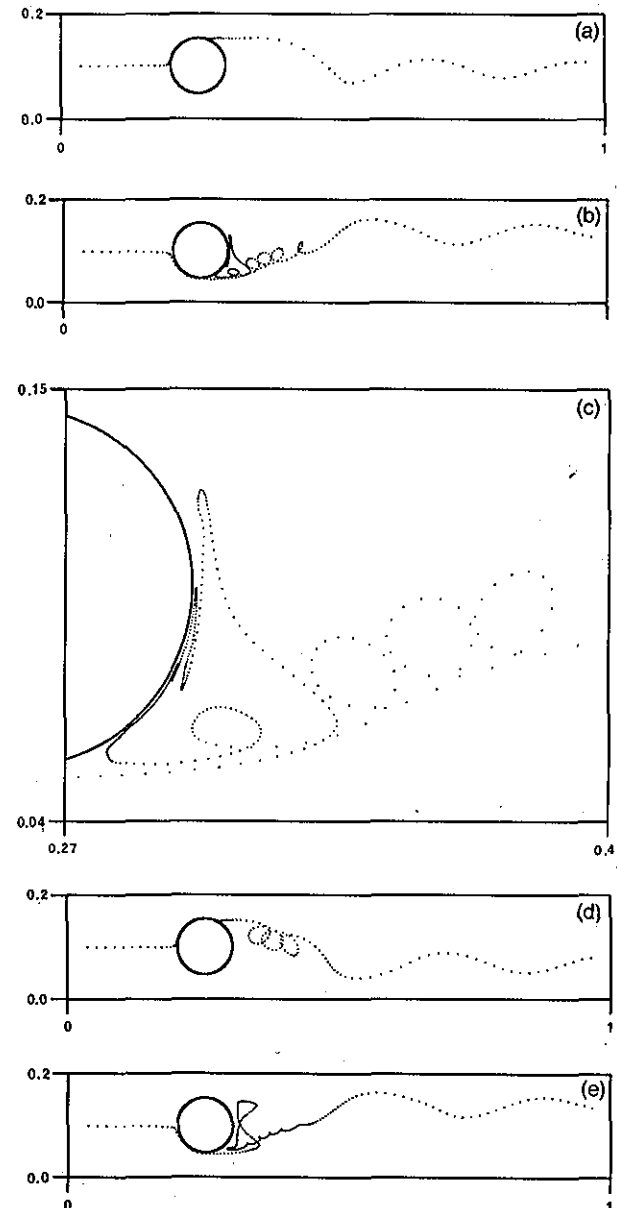


FIG. 4. Some particle trajectories in position space. Parts (a), (b), (d), and (e) show scattering trajectories with $y_{in}=0.0995$, $t_{in}=0.45$ in part (a), $t_{in}=0.35381$ in part (b), $t_{in}=0.432$ in part (d), and $t_{in}=0.3507$ in part (e). The values of Dt for these trajectories are 1.079, 2.345, 3.132, 6.405, respectively. Part (c) gives a magnification of the most interesting section of part (b).

The motion of particles inside the vortex street can be understood as follows. In time independent velocity fields, the particle trajectories coincide with the streamlines. Then it would be impossible for a particle ever to enter a vortex from the outside or to leave it from the inside. However, when the velocity field is time dependent, the positions of the vortices change against the particle and the particle can be overrun by a vortex and come inside of it. So a particle can be handed over from one vortex to the next one and stay in the region behind the cylinder for a long time, even though each individual vortex leaves this region quite rapidly. Of course, the longer a particle is supposed to remain trapped, the more precise the initial conditions of its incoming asymptote must be selected. Only for a subset of

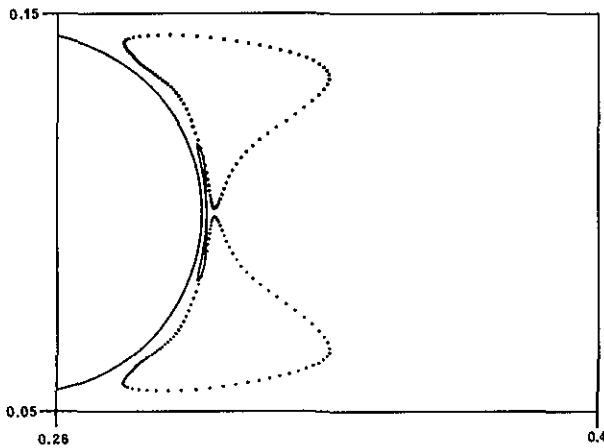


FIG. 5. Plot of the simplest periodic orbits. The two large period one orbits are drawn by dotted lines, where two consecutive points are separated by a time of $T_c/100$. The third small figure eight orbit is drawn by a solid line for better distinction.

initial conditions of measure zero can the particle be trapped among the vortices forever.

If a particle does not leave a particular vortex in time, then the particle will be carried away inside the rotating vortex performing some cycloidal motion in the laboratory frame. This type of behavior is illustrated in Fig. 4(d). Such cycloidal motion never generates infinities; it causes a cusp of finite height in the time delay function.

In order to understand the complicated behavior of long scattering trajectories, it is necessary to study the properties of periodic and localized orbits in the system. The simplest periodic orbits are plotted in Fig. 5 as dotted lines. A third period one orbit which is of figure eight shape is plotted as a solid line.

One interesting question is now: Which properties of the particle motion, and in particular of the delay function, are caused by the wall of the cylinder and which ones by the unstable periodic orbits? Can we separate these two effects? First let us have a look at the statistics of the time delay and see which of the two mechanisms dominates it. Because the trajectories we follow start and end close to the middle of the channel, they would need the time $T_0 = (x_{\text{out}} - x_{\text{in}})/1.5$ to run from x_{in} to x_{out} in the absence of the cylinder because in the asymptotic region or in the absence of the cylinder the velocity $u(x, w/2, t)$ in the middle of the channel has the value $u = 1.5$. So we define the time delay of a particle trajectory as $\delta t = DT - T_0$ where DT is the actual time the particle needed to proceed from x_{in} to x_{out} as defined above. The singularity structure in δt is of course the same as the one in DT . Then the value of δt is independent of the choice of x_{in} and x_{out} as long as these two values of x are located in the asymptotic region. We measure the number $N(\delta t)$ of particles starting in $x_{\text{in}}, y_{\text{in}}$ having a time delay larger than δt , where the initial time t_{in} is distributed evenly.

Close to the wall the tangential component of the velocity depends linearly on the distance d from the wall. Therefore, the time a particle needs to pass along the wall

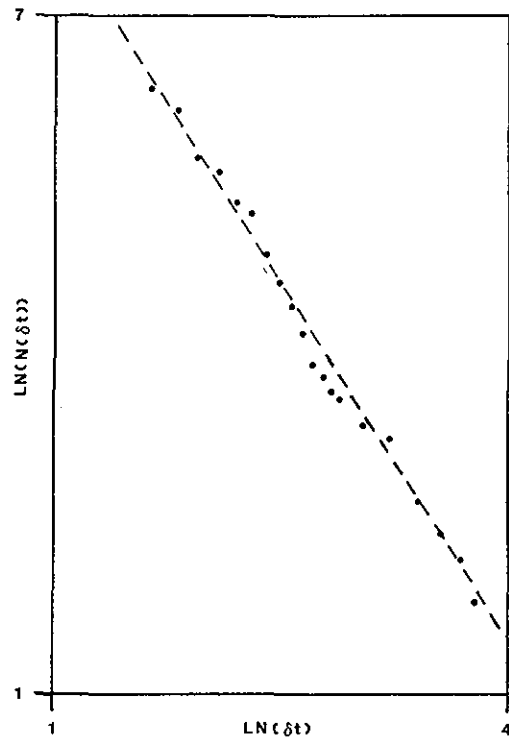


FIG. 6. Logarithm of the relative probability to find a trajectory with time delay larger than δt plotted versus $\ln(\delta t)$. The slope of the straight line is -2 . $y_{\text{in}} = 0.0995$ is kept fixed and the values of t_{in} are distributed evenly. Here $x_{\text{in}} = 0.02$ and $x_{\text{out}} = 1.0$ have been chosen. This time delay statistics was extracted from the delay function plotted in Fig. 3(b).

is proportional to $1/d$ where here d is the minimal distance from the wall. For a time independent velocity field around a cylinder, the distance of closest approach to the wall is given by $d = |b|^{1/2}$ where b is the initial impact parameter of the particle. This can easily be seen by taking into account that the ψ function grows quadratically with the radial distance from the wall. In our geometry we have $b = y_{\text{in}} - y_c$ where y_c is the coordinate of the cylinder center. We can view b as distance of the incoming asymptote from the stable manifold of the front stagnation point. If the impact parameter axis is covered evenly with incoming particles, then the relative probability to get an absolute value of the impact parameter smaller than $|b|$ is proportional to $|b|$. Accordingly, the relative probability to get a closest approach to the wall smaller than d is proportional to d^2 and the relative probability to get a delay time larger than δt is proportional to $(\delta t)^{-2}$. Now, in our case we do not have a time independent system and we do not cover the impact parameter axis (y_{in} -axis) by particles. In the time dependent system the stable manifold of the front stagnation point moves periodically in time and, therefore, an even covering of the initial time with incoming particles has the same effect as the even covering of the impact parameter in time independent systems. The probability behavior like $(\delta t)^{-2}$ is also expected in time dependent systems where the particles come in evenly distributed in time, as long as y_{in} is sufficiently close to the middle of the channel such that y_{in} is hit by the stable manifold of the

front stagnation point at some values of t_{in} . Consequently the thick stems in the time delay function shown in Fig. 3 exhibit an inverse square root singularity. Figure 6 gives a plot of $\ln(N(\delta t))$ versus $\ln(\delta t)$ extracted from the data of Fig. 3 and shows for large δt a power law decay, $(\delta t)^{-2}$.

In this sense the coarse structure of the time delay is dominated by the effects of the wall of the cylinder. The effects of the unstable periodic orbits are to be found on finer scales, especially in the internal structure of the small spikes in the wings of the main peak. Unfortunately, the numerical computations for the present case are too computationally intensive to extract the very fine effects in the time delay function. With our computer facilities we could only obtain a reliable resolution of 10^{-4} times the period T_c of the velocity field in the time delay function. To study the fine details we need a resolution up to $10^{-8}T_c$ as will be seen below.

III. THE MODEL STREAMFUNCTION

In view of the concluding comment of the previous section, let us invent an *analytical* model for the velocity field, which contains all essential ingredients of the Navier–Stokes flow and can be investigated numerically with high precision and small effort. Technically, the equation of motion of the passive particle will then be of the form of a driven Hamiltonian system with a known driving force and is of similar type as that of a driven anharmonic oscillator. Thus, because of the explicit form of the particle dynamics, a resolution several orders of magnitude better than in the original problem becomes possible.

To set up such a model, we must decide first which properties of the Navier–Stokes flow are important and must be transferred to the analytical model.

Most important are the wall of the cylinder and the linear behavior of the tangential component of the velocity close to it. To create periodic orbits we need the time dependent vortices behind the cylinder too. Also important are the background flow and its shielding directly behind the cylinder. The parabolic velocity profile of the background flow in the channel is not important, so we can choose in the analytical model a constant background flow. The walls of the channel are not important in themselves. They are only necessary to induce the following indirect effect. In a narrow channel (i.e., r is not very small compared to 1) the vortices are damped out quite rapidly and this is very useful for us since the asymptotic region is then approached quite fast by the particles. Therefore, in the analytical model we want to damp the vortices quite rapidly and let them run parallel to each other along the x -axis even though we do not include the walls of the channel explicitly.

The essential difference between the role what the walls of the channel and of the cylinder play is in the presence of stagnation points. In our case there are no stagnation points at the wall of the channel and this is why this type of boundary condition can be neglected in the model flow. At the cylinder surface, however, there are

(time periodic) attracting stagnation points present at which particles either colliding with the cylinder directly or returning to it after interacting with the vortices can come close to the surface.

By choosing the center of the cylinder to lie in the origin, we write the model streamfunction in the following form:

$$\psi(x,y,t) = f(x,y)g(x,y,t). \quad (9)$$

The first factor

$$f(x,y) = 1 - \exp(-a((x^2 + y^2)^{1/2} - 1)^2) \quad (10)$$

yields the correct boundary condition at the cylinder's surface. The cylinder radius has been taken to be unity which can always be done by suitable rescaling of the length scales. The coefficient $a^{-1/2}$ plays the role of the width of the boundary layer. This form ensures that the tangential velocity tends linearly to zero as expected in a boundary layer. The radial component of the velocity vanishes quadratically which shows that the cylinder surface can be viewed as the union of an infinite number of degenerate parabolic fixed points.

The factor g contains the contributions of the vortices and of the background flow u_0 . It reads:

$$g(x,y,t) = -wh_1(t)g_1(x,y,t) + wh_2(t)g_2(x,y,t) + u_0\psi_s(x,y). \quad (11)$$

The first two terms describe the alternating birth, evolution and damping out of vortices 1 and 2 of equal strength but opposite sign. The quantities w and $h_i(t)$ stand for the overall vortex strength and amplitudes, respectively. Because of the alternating character, one has $h_2(t) = h_1(t - T_c/2)$ where T_c denotes the time period of the flow. As a simple choice we took

$$h_1(t) = |\sin(\pi t/T_c)|. \quad (12)$$

The vortex centers are assumed to move parallel to the x -axis and with a constant velocity. Their x -coordinates [without the influence of the boundary condition prefactor $f(x,y)$] are expected to change with time as

$$x_1(t) = 1 + L[(t/T_c) \bmod 1], \quad (13)$$

$$x_2(t) = x_1(t - T_c/2) \quad (14)$$

while the y -coordinates are constants,

$$y_1(t) = -y_2(t) \equiv y_0. \quad (15)$$

Both vortices pass a distance L during time T_c and then die out. These formulas describe a situation when vortex 1 is created at $(x=1, y=y_0)$ at time zero when vortex 2 is just in its most developed state at $(x=1 + L/2, y=y_0)$. Let α denote a characteristic ratio telling us how much longer is the linear size of the vortices along the x -axis than along the y -axis. The contribution to the streamfunction of the vortices can then be expressed by the form

$$g_i(x,y,t) = \exp(-R_0[(x-x_i(t))^2 + \alpha^2(y-y_i(t))^2]) \quad (16)$$

where $R_0^{-1/2}$ is the characteristic linear size of the vortices. Note that the vortex streamfunctions are chosen to be

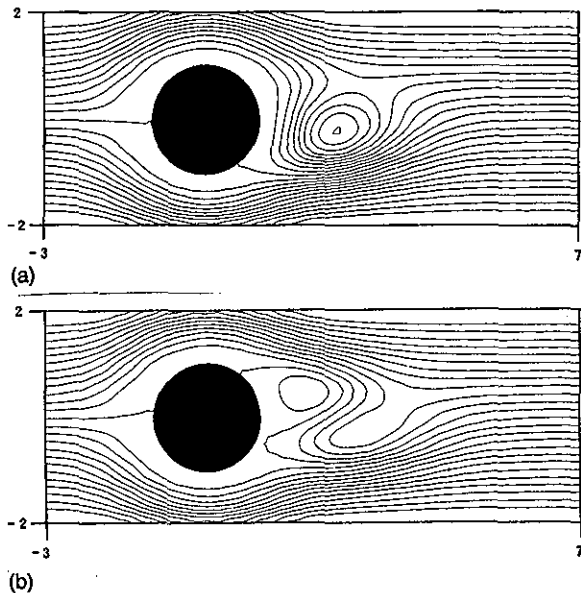


FIG. 7. Streamlines of the model flow at time $T \bmod T_c$ with $t=0$ (a) and $t=T_c/4$ (b). The parameter values in this and all the following figures are $w=0.06 \cdot T_c$, $u_0=14/T_c$, $R_0=0.35$, $\alpha=L=2$, $y_0=0.3$, $a=1$.

Gaussians of finite amplitude in contrast to the singular form used, e.g. in the theory of point vortices.

The last term in Eq. (11) gives the contribution to the streamfunction from the background flow of uniform velocity u_0 . The factor

$$s(x,y) = 1 - \exp(-(x-1)^2/\alpha^2 - y^2) \tag{17}$$

is introduced in order to simulate in a phenomenological manner the shielding of the background flow just behind the cylinder. This is taken here into account by using the same elongation factor α as in case of the vortices.

In contrast to a solution of the Navier-Stokes equations which depends only on the Reynolds number and on the aspect ratio, the model streamfunction contains several parameters. The numerical values of them are to be chosen in such a way that one obtains a phenomenological fit to a known solution of the Navier-Stokes problem. For the case of $Re=250$ and aspect ratio $r=0.25$ treated in the previous section the vortices, which had an elongation factor 2 and a maximum size of about 1.6 times the cylinder radius, disappeared at about two cylinder radius past the cylinder. Consequently, we have $\alpha=2$, $R_0=0.35$, $L=2$. We choose $y_0=0.3$. Since the vortex velocity was about 7 times slower than the background velocity, one obtains $u_0=14/T_c$. The value of $w=0.06 \cdot T_c$ was an appropriate vortex strength as it provided a considerable recirculation in the wake of the cylinder just like in the Navier-Stokes case. The parameter a determines the width of the boundary layer which in the Navier-Stokes flow is obviously different from unity. This width has essential influence on the distance of the periodic orbits from the wall of the cylinder, in a most pronounced way for the figure eight orbit, and also on their eigenvalues. In order to see a large number of hierarchical levels with good numerical precision we need small cycle eigenvalues. Therefore we take $a=1$ leading to convenient eigenvalues. At this point we definitely deviate from parameters of the

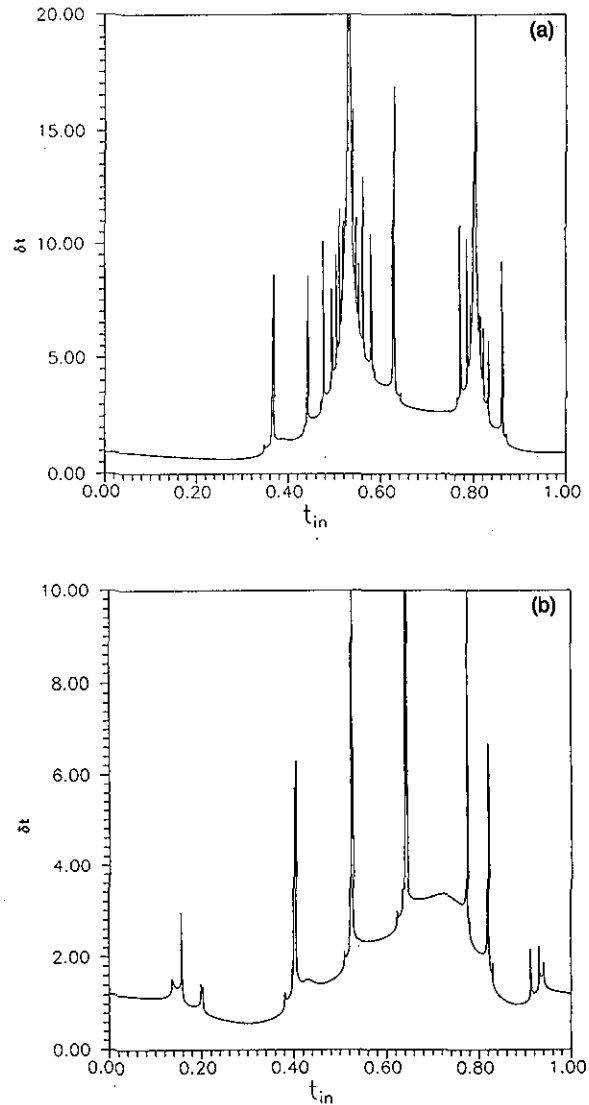


FIG. 8. Plot of the time delay function $\delta t(t_{in})$ for the model flow for two different initial points in position space: $(x_{in}, y_{in}) = (-5, 0.01)$ in part (a) and $(x_{in}, y_{in}) = (-5, 0.015)$ in part (b). We have used $x_{out} = 10$.

Navier-Stokes flow but, as we shall see, the results do not depend essentially on the particular value of a and our choice was motivated just by numerical convenience. The smooth form of the shielding function [see Eq. (17)], which is much softer than the one appearing in the Navier-Stokes flow, has been chosen for similar reasons.

Figure 7 shows the streamlines obtained from ψ of Eqs.(9)-(17) at times $t=0$ and $t=T_c/4$ which are to be compared with the corresponding plots of the Navier-Stokes flow given in Fig. 2. In the following we measure all times in units of T_c .

The time delay function δt versus t_{in} is plotted in Fig. 8 for two different initial points, where $\delta t = T - T_0$, $T_0 = (x_{out} - x_{in})/u_0$. In the first case the stable manifold of the front stagnation point is obviously met and generates the two strong singular stem-like structures. Their overall shape has an inverse square root behavior on which sharp spikes, the fingerprints of the periodic orbits, are superimposed. We could not resolve the latter in the Navier-Stokes

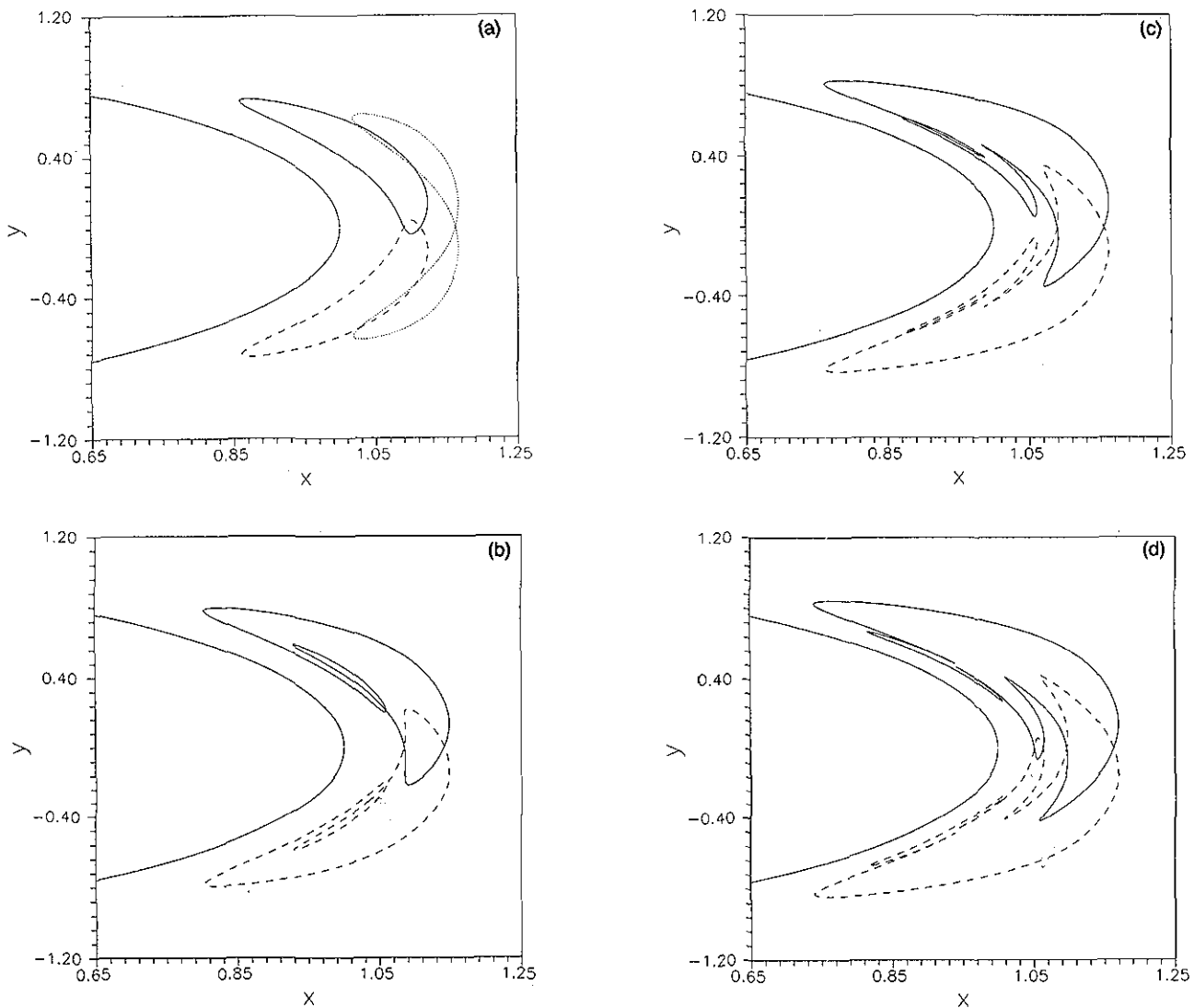


FIG. 9. Plot of the shortest periodic orbits in the model flow. Part (a) shows three different orbits of period one. Parts (b), (c), and (d) exhibit two symmetry related orbits of period 2, 3, and 4, respectively. Note the different scales along the axes which were chosen in order to have better visualization.

simulation. The similarity with the corresponding structures in Fig. 3 for the Navier–Stokes flow is striking. In part (b) y_{in} is sufficiently far away from the middle axis such that the front stagnation point is not met by trajectories starting from here, regardless of the initial time. Nevertheless, trajectories can come to the vicinity of the front stagnation point but not arbitrarily close to it which causes a finite amount of time delay. This amount is in our example no more than about 3.5 which corresponds to the height of the highest plateau on the plot. Consequently, we only see now a truncated stem. It looks as if in Fig. 8(a) the main stems would have been cut at a relatively low level. Here the nonhyperbolic influences are less pronounced and such initial conditions are good candidates for analyzing the influence of hyperbolic periodic orbits on the time delay. The spikes, i.e. points where the time delay diverges, are caused by trajectories which come into the vortices and run close to periodic orbits for a while or are pushed close to the rear stagnation point of the cylinder by the recirculation. Note that cusps caused by cycloidal mo-

tion also appear in Fig. 8 just like in the Navier–Stokes flow. The most pronounced one can be seen at $t_{in}=0.16$ in Fig. 8(b).

IV. PERIODIC ORBITS

By the application of Newton's method to the stroboscopic map of the particle dynamics, obtained by taking snapshots at integer multiples of the time period, we managed to determine the shortest and simplest periodic orbits. Figure 9 shows them in the position space. Part (a) exhibits three different orbits of period one. Two of them (solid and dashed line) are mirror images of each other. In spite of this geometrical symmetry, we need both of them as independent basic blocks to shadow long periodic orbits and scattering trajectories. These two orbits are hyperbolic and have eigenvalues $\Lambda_1 = -5.3$. Here and in the following, by eigenvalue of a periodic orbit we mean the eigenvalue largest in modulus of the linearized dynamics of the stroboscopic map around the periodic point corresponding

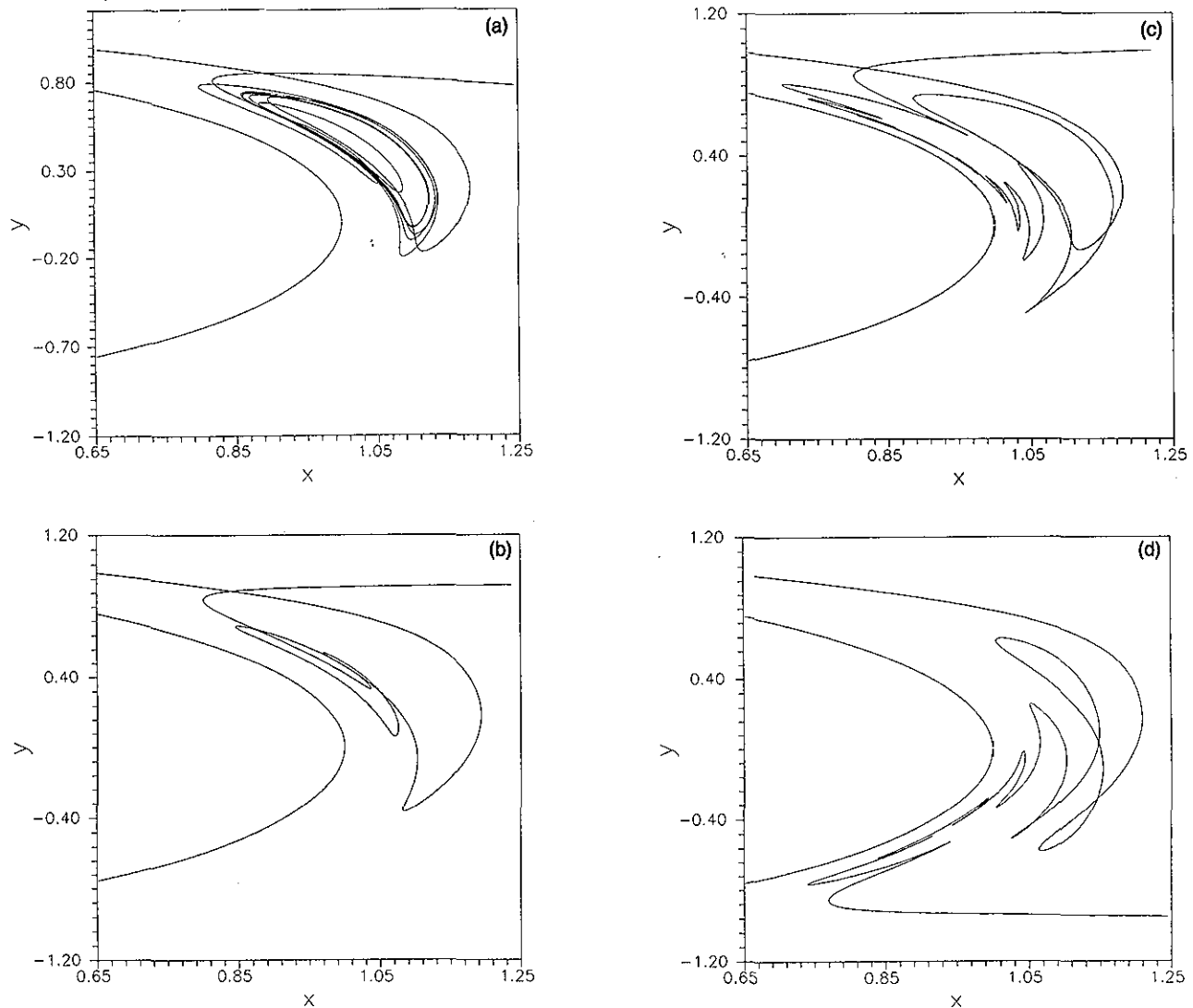


FIG. 10. Four different scattering trajectories. The initial coordinates are the same $(x_{in}, y_{in}) = (-5, 0.015)$ in all cases, while the initial times are $t_{in} = 0.4054457, 0.4035, 0.4058,$ and 0.40114 in parts (a), (b), (c) and (d), respectively. The corresponding time delays are $\delta t = 9.10, 3.77, 10.63,$ and 7.23 . Frame and scale are the same as in Fig. 9.

to this periodic orbit. As a further orbit of period one we found a figure eight shaped orbit [dotted line in Fig. 9(a)] having eigenvalue $M=24$. Note that this number is on the order of Λ_1^2 which means that the half of this orbit plays a similar role as any one of the other two period one orbit. The topology of these cycles is the same as for the corresponding ones in the Navier–Stokes flow. The exact shape and their distance from the wall differ due to the smoother form of the shielding of the background flow behind the cylinder and due to the broader boundary layer. This is in accordance with the fact that the eigenvalues of the period one orbits in the Navier–Stokes flow were so big (on the order of 1000) that their precise determination was impossible. This is also why higher period orbits could not be identified in that case.

In the model flow a sequence of period 2, 3 and 4 orbits have been found [Figs. 9(b)–9(d)] which come with increasing period closer and closer to the wall. Their form suggests that they can be shadowed by a period one orbit

and segments lying close to the wall. When computing their eigenvalues, we found $\Lambda_2 = -21, \Lambda_3 = -65, \Lambda_4 = -108$. The evaluation of the corresponding Lyapunov exponents $\lambda_n = \ln(|\Lambda_n|)/n$ shows a decrease with the period. We obtain: $\lambda_1 = 1.67, \lambda_2 = 1.53, \lambda_3 = 1.39,$ and $\lambda_4 = 1.17$. By taking into account that the wall is the union of degenerate parabolic points with Lyapunov exponent zero, we can conclude that the wall plays the role of a basic periodic orbit of marginal stability. In this respect it is similar to a KAM surface. The boundary of the latter one is a complicated fractal structure in contrast to the surface of the cylinder. Both objects induce a nonexponential decay in the time delay statistics described by a power law $(\delta t)^{-\sigma}$. In the case of KAM tori the decay is slower because of their stickiness. The theoretical prediction $\sigma \approx 1.5$ (Refs. 30–35) has been confirmed by a recent experiment.³⁶ This σ differs from the exponent $\sigma = 2$ characterizing the smooth surface of the cylinder derived in Sec. II.

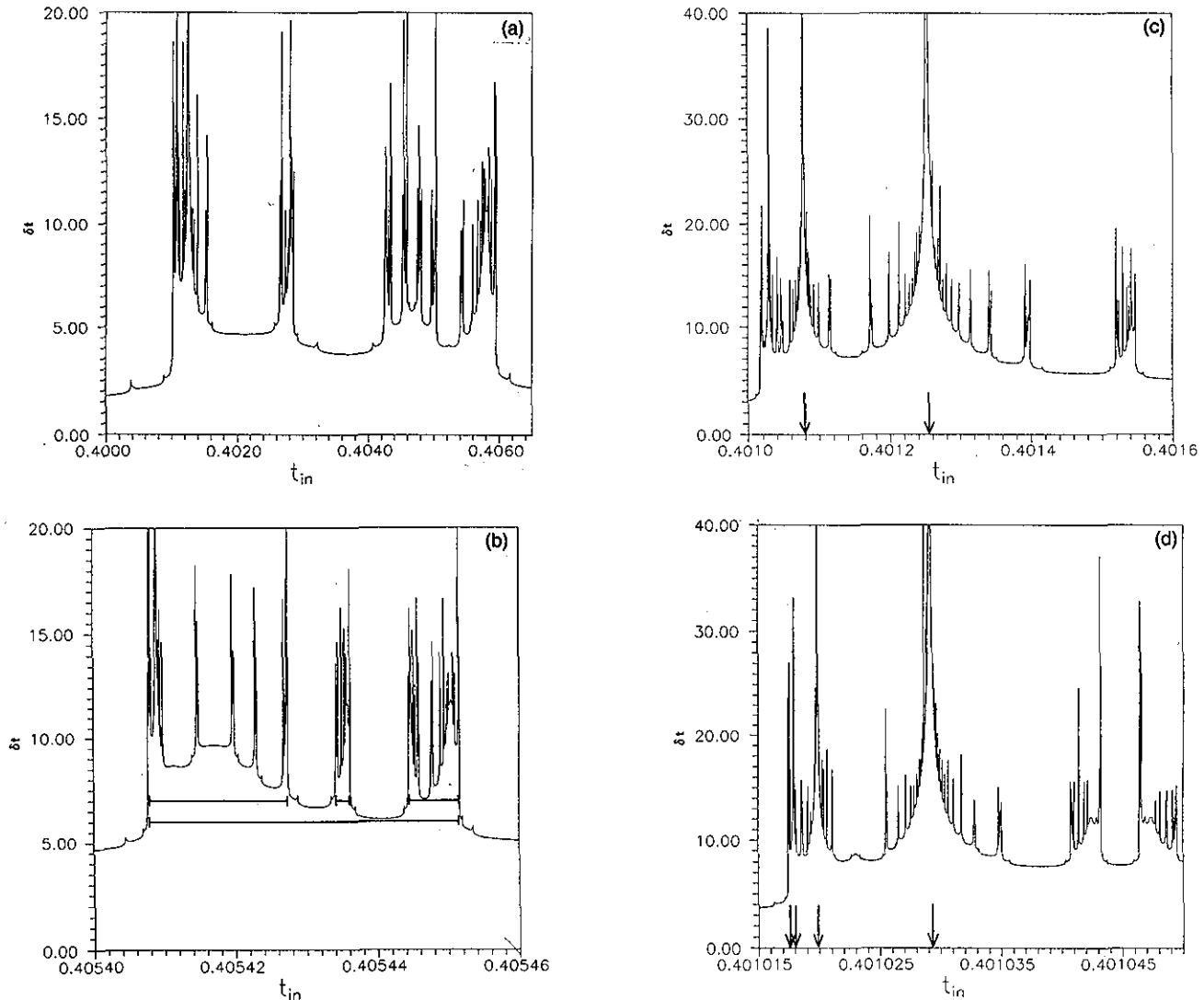


FIG. 11. Plot of four magnifications of the time delay function showed in Fig. 8 (b). In part (b) the threshold lines $\delta t=6$ and $\delta t=7$ are inserted in order to illustrate how the time delay function cuts out intervals on the t_{in} axis such that (i) the end points are infinities, (ii) the value of δt is always larger than the given threshold in the interiors. The lengths $I_i^{(n)}$ of these intervals are the inputs into the thermodynamical formalism [see Eq. (18)]. Note the self-similar structures in parts (c) and (d). The arrows indicate the values of t_{in} which belong to the scattering trajectories plotted in Fig. 12. The resolution needed to plot part (d) was 10^{-8} times the period.

In analogy with nonhydrodynamical scattering processes, periodic orbits have an essential influence on long-lived scattering trajectories. In our system there are two qualitatively different possibilities: (i) the scattering trajectory comes close to one of the periodic orbits like the ones given in Figs. 10(a) and 10(b), which approach a period one and period two orbit shown in Figs. 9(a) and 9(b), respectively. (ii) The scattering trajectory comes close to the wall either directly or after having visited a periodic orbit. Figures 10(c) and 10(d) exhibit examples with two different period one orbits. The second possibility leads to much longer time delays because of the marginal stability of the wall, and is responsible for the power law behavior in the time delay statistics. This observation confirms again our belief that the wall acts like a periodic orbit.

V. THE STRUCTURE OF THE TIME DELAY FUNCTION

As seen in Sec. III, one has a better opportunity for studying finer details of the time delay function if initial

conditions are taken which avoid a direct collision with the front stagnation point. Figure 8(b) shows such a situation, where we plotted the time delay δt versus t_{in} . The narrow spikes in the figure correspond to trajectories being trapped in a region behind the cylinder.

The magnification of the spikes provides information about the mechanisms causing long delay times. Figure 11(a) exhibits a magnification of the first spike in Fig. 8(b) around $t_{in}=0.4$. One discovers in this picture both complete and truncated stems again which correspond now to an exact collision with or passing nearby the rear stagnation point. An example of an incomplete stem can be seen around $t_{in}=0.406$. More truncated stems show up in a next level magnification in Fig. 11(b). Notice the qualitative similarity between any truncated stem and the global structure of Fig. 8(b).

Complete stems also appear in these pictures like for example the one lying at $t_{in}=0.4012$ in Fig. 11(a). To

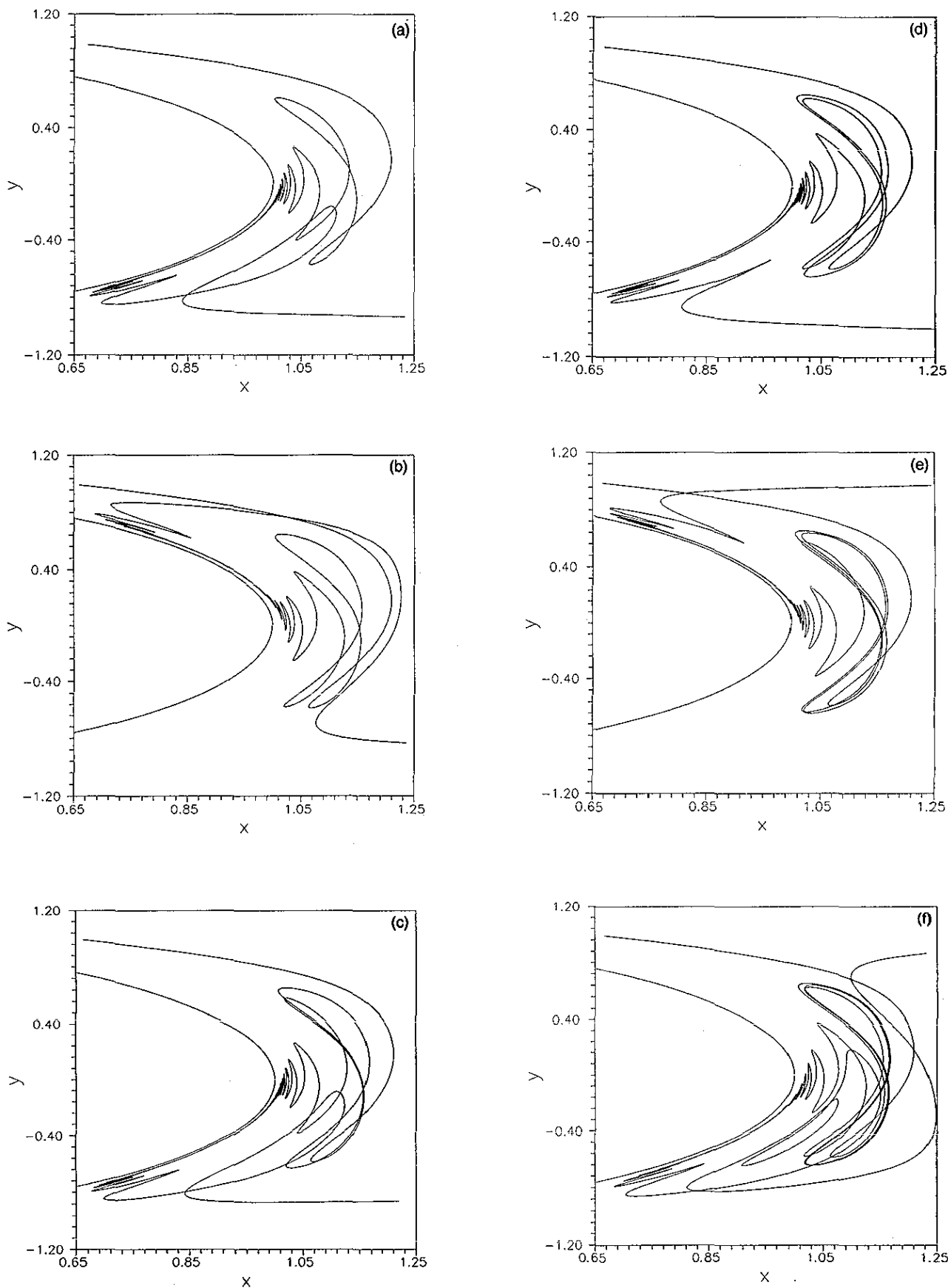


FIG. 12. Six scattering trajectories starting at $(x_{in}, y_{in}) = (-5, 0.015)$ in all cases, while the initial times are $t_{in} = 0.40125, 0.401075, 0.401029, 0.4010199, 0.40101795,$ and 0.40101755 , in parts (a)–(f). They follow the figure eight orbit for longer and longer times before reaching the wall near the attractive rear stagnation point. The corresponding time delays are $\delta t = 29.24, 17.33, 32.42, 32.12, 26.69,$ and 22.74 . Frame and scale are the same as in Fig. 9.

study their organization, we performed in Figs. 11(c) and 11(d) a subsequent magnification of the leftmost cluster of singularities which leads to a striking self-similarity. One can read off these pictures that the sequence of complete stems converges to the left boundary of the cluster at $t_{in}=0.4010175$ according to a geometrical progression. (The weight of these singularities also follows a geometrical progression.) The asymptotic scaling factor of the progression is about 4.8.

The origin of this factor can be understood by taking trajectories from the inside of stems in this sequence. Figures 12(a)–12(f) shows the first six members of the sequence. All trajectories approach the rear stagnation point, move for a long time along the wall, and escape at one of the unstable stagnation points. If the initial point lies exactly in the middle of the stem, the trajectory collides with the rear stagnation point and stays there forever. For other initial conditions inside the stem the lifetime is long but finite, and whether escape takes place at the lower or upper unstable stagnation point depends on which half of the stem the trajectory started from. In this sequence of figures, trajectories come close to the figure eight orbit before reaching the wall. Two consecutive members of the sequence differ by performing an additional half-revolution around this orbit of period one. In order to perform one additional half-revolution, the distance of the initial conditions from the stable manifold of this periodic orbit must be smaller by a factor $M^{1/2}=4.89$. This explains the scaling properties found above. In addition it explains why the background value of the time delay rises by 1/2 from any stem to the next one in this sequence.

After leaving the wall at one of the unstable stagnation points, the trajectory can come close to a periodic orbit again. In Figs. 12(a) and 12(c) the outgoing trajectory performs one loop around the lower period one orbit and in Fig. 12(f) one loop around the lower period two orbit. With higher numerical precision we could even find trajectories leaving the wall, performing any sequence of loops around periodic orbits, coming close to the wall again, etc. All these possibilities create singularities in the time delay function, which are fine spikes on the slope of the stem. Thus, in each neighborhood of any singularity one finds an arbitrary number of complete stems on sufficiently small scales. The set of complete stems contains sequences characterized by scaling factors coinciding with eigenvalues of any periodic orbit. In the case of the figure eight orbit we found the square root of the eigenvalue and not the eigenvalue itself which is due to the symmetry of this periodic orbit.

The complete stems have a shape of a one over square root singularity in this case, too, which leads asymptotically to a power law behavior in the time delay statistics $(\delta t)^{-\sigma}$ with $\sigma=2$ according to the discussion in Sec. II.

These observations support the view that the invariant set can be split into a hyperbolic and a nonhyperbolic component. The first one consists of those periodic orbits which are all well separated from the wall, and the homoclinic and heteroclinic intersections among them, while the second one contains all elements which are essentially influ-

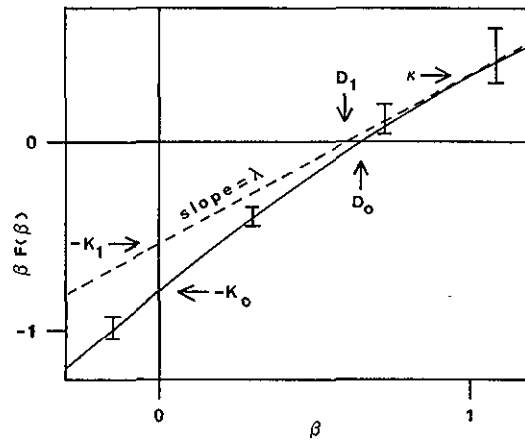


FIG. 13. The free energy computed from Eq. (19). The way how interval lengths were determined is illustrated in Fig. 11(b). The analysis is based on levels $n=4$ to 8. The error bars indicate the fluctuations found in this range of n . The dashed line is tangent to the graph of $\beta F(\beta)$ at $\beta=1$.

enced by the wall. The short time behavior of the system can then be explained in terms of the hyperbolic part, and is dominated on longer time scales by the nonhyperbolic effects.

VI. QUANTITATIVE CHARACTERIZATION OF THE HYPERBOLIC PART

After having seen that the eigenvalues of the periodic orbits appear in the time delay function, it is natural to use methods for characterizing the chaoticity of the scattering process worked out for hyperbolic systems. The application of the thermodynamic formalism has turned out to be powerful in the case of chaotic scattering, too. The essential input of this approach are intervals ending at two singularities. They are defined²³ such that the time delay on these intervals has to be larger than or equal to a threshold value. Threshold values differing by integer multiples of the period T_c are taken. This method opens up a level structure in the time delay function as illustrated by Fig. 11(b). The central object, the free energy $F(\beta)$ is extracted from the interval lengths $l_i^{(n)}$ at level n by applying the formula

$$\sum_i (l_i^{(n)})^\beta \sim e^{-\beta F(\beta)n} \quad (18)$$

valid for large values of n where the number of intervals is also very large. The weighting exponent β , playing the role of an inverse temperature, can be any real number. Numerically we computed the partition sum $Z(n,\beta) = \sum_i (l_i^{(n)})^\beta$ for different values of n and approximated the free energy according to

$$\beta F(\beta) \approx -\ln Z(n,\beta) + \ln Z(n-1,\beta). \quad (19)$$

Fortunately the convergence of the right hand side is exponentially fast in the hyperbolic range and one finds a reliable value of the free energy extracted at low levels of n . The fluctuations of the right-hand side of Eq. (19) in n can be considered as a measure of the uncertainty.

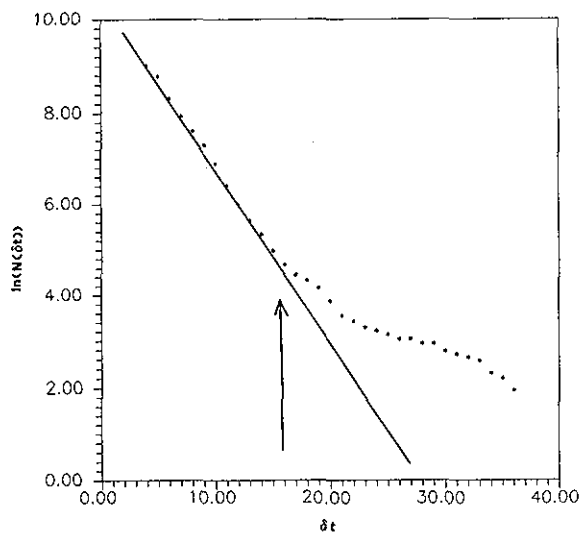


FIG. 14. Logarithm of the relative probability to find a trajectory with time delay larger than δt plotted versus δt . This time delay statistics corresponds to the delay function plotted in Fig. 8(b). The straight line represents the best linear fit to the short time decay with a slope of -0.38 . The arrow indicates the crossover value δt_c to the algebraic behavior.

Important characteristics of the hyperbolic part can be read off the function $\beta F(\beta)$.²³ In particular: The topological entropy K_0 , i.e., the growth rate of the number of intervals, follows from the intersection with the vertical axis as $K_0 = -\beta F(\beta)|_{\beta=0}$. The fractal dimension D_0 is obtained from the intersection with the horizontal axis: $F(\beta = D_0) = 0$. The escape rate κ , whose reciprocal value is the average chaotic lifetime, and the Lyapunov exponent λ are obtained as the value and the slope of $\beta F(\beta)$ taken at $\beta = 1$, respectively. The line tangent to $\beta F(\beta)$ at $\beta = 1$ intersects the vertical and horizontal axis at the value of the metric entropy K_1 times (-1) and at the value of the information dimension D_1 , respectively. This is a geometrical expression of the relation³⁷

$$K_1 = \lambda - \kappa = D_1 \cdot \lambda. \quad (20)$$

We applied the thermodynamic approach to low level lines of the time delay function. Since nonhyperbolic effects start to appear around $n=10$, we studied the levels $n=4, \dots, 8$. The result obtained for the free energy is plotted in Fig. 13 together with the error bars. Thus, we conclude that the hyperbolic part is characterized by the values $K_0=0.8$, $D_0=0.65$, $\kappa=0.35$, $\lambda=0.9$. For the metric entropy and the information dimension we obtain $K_1=0.55$ and $D_1=0.6$, respectively. Because of the low lying levels the relative accuracy is about 0.05 in the range investigated. It is worth mentioning that the average Lyapunov exponent λ is approximately the half of the instability exponent λ_1 of the period one orbit. This can be interpreted by recalling that the largest and the smallest instability exponent belong to the period one orbit (see Sec. III) and to the wall, respectively. As the wall is marginally stable, the averaged Lyapunov exponent is close to the algebraic mean of the local Lyapunov exponents.

As an independent check we measured the fractal dimension of the singularities in the time delay function by the so-called sandbox method³⁸ giving a value of $D_0=0.60$. We also measured the time delay statistics directly from the short time exponentially decaying part and extracted from the first exponential part $\kappa=0.38$. Figure 14 shows the plot of the logarithm of the number of trajectories with delay time larger than δt as a function of δt extracted from the data of Fig. 8(b). In the analysis only intervals lying above $\delta t=4$ have been taken into account. Thus the effect of the main stem which is cut at $\delta t=3.5$ has been disregarded. Trajectories have been sampled with a resolution of $2.5 \cdot 10^{-6}$ in t_{in} . Note that the exponential behavior breaks down at about $\delta t=15$. On longer scales the power law decay caused by the collision of trajectories with the rear stagnation point takes over. This is in accordance with the observation that many spikes in Fig. 11 disappear around $\delta t=15$ and only complete stems survive for higher values.

We note that the thermodynamical formalism can be applied to the nonhyperbolic part as well. Because of the presence of interval lengths shrinking slower than exponentially (e.g., interval lengths defined by complete stems), the free energy would be identically zero for $\beta \geq 1$, just like in point mechanical systems with divided phase spaces.³⁹ From the general relations then follows that the escape rate and the Lyapunov exponent vanish and the fractal dimension becomes 1 in this case.⁴⁰

VII. CONCLUSIONS

We investigated here a dynamical system which arose from a hydrodynamical problem. It was shown that the advection of passive particles in open flows corresponds to scattering processes which are typically chaotic. The gross features of the problem can well be understood by a direct simulation of the Navier–Stokes flow, but in order to study the fine details an analytical model was useful for us. The main conclusion we draw from the analytical model is that the *boundary conditions* applied to the flow have a drastic effect on the dynamical system. They lead to the appearance of a *smooth torus* in phase space which is in the hydrodynamical problem the surface of the obstacle. The presence of this torus leads to a nonhyperbolic behavior expressed by the appearance of a power law in the time delay statistics $(\delta t)^{-\sigma}$ with $\sigma=2$. A similar power law could be generated by KAM tori but then the decay should be slower because they are more sticky for neighboring trajectories. In our simulation we have not found any sign of KAM surfaces but cannot exclude their existence on very fine scales.

By a careful analysis of the time delay function one can separate hyperbolic and nonhyperbolic effects. The first can be observed on short time scales and reflects the presence of an infinity of strictly unstable periodic orbits. Methods worked out for characterizing hyperbolic point mechanical scattering processes can well be applied in this range. The long time behavior is dominated by the nonhyperbolic effect of the wall. The crossover can clearly be seen in the time delay statistics, too, where it separates

regions with exponential and power law decays. The cross-over value δt_c can strongly depend on the choice of initial conditions in position space. In the case of Fig. 8(a) it is close to 2 and an exponential decay cannot be observed at all, while in Fig. 8(b) $\delta t_c \approx 15$ because initial conditions are there chosen in such a way that a quick collision with the stagnation points is avoided. We note that such a cross-over behavior can be present due to the KAM surfaces in any point mechanical scattering process.⁴¹

The surface of the smooth torus, i.e., the wall of the obstacle, is the union of an infinity of degenerate parabolic points. The wall acts as a periodic orbit with marginal stability and has to be included as a basic block in constructing scattering trajectories via the shadowing principle.

It is worth mentioning that the effects found in this hydrodynamical problem can be present in any point mechanical scattering process where the invariant set contains one or more isolated orbits of marginal stability, like, e.g., bouncing motion between two parallel walls of an open billiard.

We have restricted our attention up to now to flows in two-dimensional position space. The passive transport in incompressible flows possesses a direct analogy with Hamiltonian dynamics. We conclude with a few remarks on the more realistic three-dimensional case. The Hamiltonian analogy is no longer complete because of the odd dimension of the phase space. Nevertheless, incompressibility implies phase volume conservation. Another new feature is that in three dimensions even time independent flows can create chaotic advection^{9,11} which in open flows leads to chaotic scattering.¹⁶ The general features are expected, however, to be the same as of the system studied above: the time delay function should exhibit complicated structures, the presence of the boundary condition at the surface of the obstacle should induce nonhyperbolic effects. Even in three-dimensional time periodic cases, the dimension of the extended phase space (having a value 4) is not large enough to produce the hiding of the chaotic set which can occur for point mechanical motion in three-dimensional position space.⁴² We expect, therefore, that the passive transport around three-dimensional obstacles is qualitatively the same as in two-dimensional cases.

ACKNOWLEDGMENTS

One of the authors (C. J.) thanks the Deutsche Forschungsgemeinschaft for financial support in form of a Heisenberg stipendium. This work has partially been supported by the Hungarian Scientific Research Foundation under Grant Nos. OTKA 2090 and OTKA T4439 and by the Foundation for Higher Education and Research. The authors are indebted to A. Péntek and Z. Toroczkai for a critical reading of the manuscript. We thank Professor S. Albeverio for his support for this work. The fluid dynamical computer program was constructed originally for the Priority Project "Finite Approximations in Fluid Dynamics" under the coordination of Professor E. Krause. The

Navier–Stokes flow computations have been done on the vector computer CDC-205 and the scalar computer CDC-992 of the Computer Center of the University Bochum. We thank the staff of the Computer Center and Dr. R. Mannshardt for their support.

- ¹E. A. Novikov and Y. B. Sedov, *Sov. Phys. JETP* **48**, 440 (1978); *JETP Lett.* **29**, 677 (1979); H. Aref and N. Pomphrey, *Phys. Lett. A* **78**, 297 (1980); J. Manakov and L. Schur, *JETP Lett.* **37**, 54 (1983); H. Aref, *Annu. Rev. Fluid Mech.* **15**, 345 (1983); *J. Fluid Mech.* **143**, 1 (1984); E. A. Novikov, *Phys. Lett. A* **112**, 327 (1985).
- ²J. Chaiken, C. K. Chu, M. Tabor, and Q. M. Tan, *Phys. Fluids* **30**, 687 (1987).
- ³J. M. Ottino, *The Kinematics of Mixing: Stretching, Chaos, and Transport* (Cambridge U.P., Cambridge, 1989).
- ⁴H. Aref, *Philips. Trans. R. Soc. London* **333**, 273 (1990); V. Rom-Kedar, A. Leonard, and S. Wiggins, *J. Fluid. Mech.* **219**, 347 (1990).
- ⁵J. M. Ottino, *Annu. Rev. Fluid. Mech.* **22**, 207 (1990).
- ⁶A. Provenzale, A. R. Osborne, A. D. Kirwan, and L. Bergamasco, in *Nonlinear Topics in Ocean Physics*, edited by A. R. Osborne (Elsevier, Amsterdam, 1991).
- ⁷A. Crisanti, M. Falcioni, G. Paladin, and A. Vulpiani, *Riv. Nuovo. Cimento* **14**, 1 (1991).
- ⁸F. J. Muzzio, P. D. Swanson, and J. M. Ottino, *Int. J. Bifurc. Chaos* **2**, 37 (1992).
- ⁹Y. T. Lau and J. M. Finn, *Physica D* **57**, 283 (1992).
- ¹⁰K. Ouchi and H. Mori, *Prog. Theor. Phys.* **88**, 467 (1992).
- ¹¹A. A. Chernikov and G. Schmidt, *Phys. Lett. A* **169**, 51 (1992).
- ¹²J. C. Sommerer and E. Ott, *Science* **259**, 335 (1992).
- ¹³L. Yu, E. Ott, and Q. Chen, *Phys. Rev. Lett.* **65**, 2935 (1990).
- ¹⁴L. Yu, E. Ott, and Q. Chen, *Physica D* **53**, 102 (1991).
- ¹⁵S. Jones and H. Aref, *Phys. Fluids* **31**, 469 (1988) [for early attempts see A. E. Perry, M. S. Chong, and T. Lim, *J. Fluid Mech.* **116**, 77 (1982); R. W. Davis and E. T. Moore, *ibid.* **116**, 475 (1982)].
- ¹⁶S. Jones, O. Thomas, and H. Aref, *J. Fluid. Mech.* **209**, 335 (1989); W. R. Young and S. W. Jones, *Phys. Fluids A* **3**, 1087 (1991); S. W. Jones and W. R. Young, *J. Fluid. Mech.* (in press).
- ¹⁷K. Shariff, T. H. Pulliam, and J. M. Ottino, *Lect. Appl. Math.* **28**, 613 (1991).
- ¹⁸C. Jung and E. Ziemniak, *J. Phys. A* **25**, 3929 (1992).
- ¹⁹S. Bleher, C. Grebogi, and E. Ott, *Physica D* **46**, 87 (1990).
- ²⁰U. Smilansky, in *Chaos and Quantum Physics*, edited by M.-J. Gannoni, A. Voros, and J. Zinn-Justin (Elsevier, New York, 1992).
- ²¹T. Tél, in *Directions in Chaos*, edited by B. Hao (World Scientific, Singapore, 1990), Vol. 3, pp. 149–221.
- ²²C. Jung, *Acta. Phys. Polonica* **23**, 177 (1992).
- ²³Z. Kovács and T. Tél, *Phys. Rev. Lett.* **64**, 1617 (1990).
- ²⁴T. Tél, *Phys. Rev. A* **44**, 1034 (1991).
- ²⁵T. Tél, *J. Phys. A* **22**, L691 (1989).
- ²⁶P. Cvitanović and B. Eckhardt, *Phys. Rev. Lett.* **63**, 823 (1989).
- ²⁷C. Jung and P. Richter, *J. Phys. A* **23**, 2847 (1990).
- ²⁸F. H. Harlow and J. E. Welch, *Phys. Fluids* **8**, 2182 (1965).
- ²⁹B. Eckhardt and C. Jung, *J. Phys. A* **19**, L829 (1986).
- ³⁰C. F. Karney, *Physica D* **8**, 360 (1983).
- ³¹J. D. Meiss and E. Ott, *Phys. Rev. Lett.* **55**, 2741 (1985).
- ³²M. Ding, T. Bountis, and E. Ott, *Phys. Lett. A* **151**, 395 (1990).
- ³³Y. Lai, R. Blümel, E. Ott, and C. Grebogi, *Phys. Rev. Lett.* **68**, 3491 (1992).
- ³⁴Y. Lai, C. Grebogi, R. Blümel, and M. Ding, *Phys. Rev. A* **45**, 8284 (1992).
- ³⁵C. F. Hillermeier, R. Blümel, and U. Smilansky, *Phys. Rev. A* **45**, 3486 (1992).
- ³⁶T. H. Solomon, E. R. Weeks, and H. L. Swinney, *Phys. Rev. Lett.* (in press); M. S. Pervez and T. H. Solomon (preprint, 1993).
- ³⁷H. Kantz and P. Grassberger, *Physica D* **17**, 75 (1985).
- ³⁸T. Tél, A. Fülöp, and T. Vicsek, *Physica A* **159**, 155 (1989).
- ³⁹W. Breyermann, Z. Kovács, and T. Tél, "Chaotic scattering in external magnetic fields" (preprint, 1993).
- ⁴⁰Y. T. Lau, J. M. Finn, and E. Ott, *Phys. Rev. Lett.* **66**, 978 (1991).
- ⁴¹Y. C. Lai, T. Tél, and C. Grebogi, *Phys. Rev. E* **48**, 709 (1993).
- ⁴²Q. Chen, M. Z. Ding, and E. Ott, *Phys. Lett. A* **145**, 93 (1990).